Mussatayev, M., Yi, Q., Fitzgerald, M., Maes, V. K., Wilcox, P., & Hughes, R. (2023). *Directional eddy current probe configuration for in-line detection of out-of-plane wrinkles*.

Early version, also known as pre-print

Link to publication record in Explore Bristol Research
PDF-document

Directional eddy current probe configuration for in-line detection of out-of-plane wrinkles

Meirbek Mussatayev[1][*], Qiuji Yi [1,2], Mark Fitzgerald [3], Vincent K. Maes[2], Paul Wilcox[1], Robert Hughes[1]

[1] Department of Mechanical Engineering, Ultrasonics and Non-destructive Testing (UNDT), University of Bristol, Bristol BS8 1TR, U.K.

[2] Department of Aerospace Engineering, Bristol Composites Institute (ACCIS), University of Bristol

[3] Electrical Workshop, Engineering Faculty Office, University of Bristol

Highlights:

- Development of lift-off insensitive eddy-current sensors for in-line wrinkle detection.

- Implementation of new finite-element modelling shows prediction of most effective probe configuration.

- Samples with complex out-of-plane wrinkle morphologies were manufactured and tested.

- High defect detection with SNR >20 for wrinkles with amplitude of 1.3 mm.

- Sensor configurations can be selected for insensitivity to skewness.

Abstract: Real-time monitoring of carbon fibre composites during Automated Fibre Placement (AFP) manufacturing remains a challenge for non-destructive evaluation (NDE) techniques. An directional eddy-current (EC) probe with asymmetric transmit and differential receive (Tx-dRx) coils is designed, constructed and characterized to evaluate the detectability of out-of-plane wrinkles. Initial studies were conducted to determine suitable excitation frequencies and to analyse the impact of relative orientations of driver and pickup coils on wrinkle detectability. The probe configurations are evaluated experimentally and employ a new finite element modelling approach to better understand the relationship between eddy-current density and defect detection. The findings indicate that a probe configuration with an asymmetric driver coil normal to the material surface and aligned with the fibre directions, and with differential pickup coils 90 degrees to the scanning direction, shows the best capability for out-of-plane wrinkle detection, with SNR >20 for wrinkles over 1.3 mm in amplitude.

* Corresponding author. Department of Mechanical Engineering, Ultrasonics and Non-destructive Testing (UNDT), University of Bristol, BS8 1TR, UK. E-mail address: meirbek.mussatayev@bristol.ac.uk (M. Mussatayev).

1

1   Introduction

Carbon fibre reinforced polymer (CFRP) composite materials are made from high-strength carbon fibres embedded in the flexible and tough epoxy matrix. They are widely used and attractive for many industrial applications because of their superior mechanical properties in comparison with its conventional counterparts [1]–[3]. CFRP provides the best of both worlds - high strength from carbon fibres, with flexibility and toughness from the epoxy matrix. CFRP engineering components are regularly manufactured by stacking several ply laminate layers, with distinct fibre orientations, to obtain suitable mechanical properties along desired load paths. The exponential growth in demand for CFRP production over the past decade from 2010 to 2020, and predictions of further growth in global demand by 2050 [4] is clear evidence for the need to increase automated production rates.

Automated fibre placement (AFP) and automated tape layup (ATL) are the most common methods of CFRP production, offering minimal material scrap, low labor costs and high repeatability, accuracy and productivity in comparison with manual composite manufacturing methods [5]. The current challenge in AFP-based manufacturing processes is the accurate inspection and quality monitoring of the as-laid material – something currently performed by qualitative and subjective manual visual methods.

The following subsections outline the proposed concept requirements, the state-of-the-art of in-line Non-Destructive Evaluation (NDE) techniques for in-line monitoring of automated manufacturing and the analysis of suitable NDE approach for a targeted defect type.

1.1   Conditions for real-time quality control in AFP systems

Any potential in-line inspection technique for AFP manufacturing should meet the following prerequisites:

1.   Non-contact - to prevent the introduction of contact damage or foreign contaminants into the layup structure.

2.   Compatibility with AFP process environments - i.e. high deposition speeds (0.1-1 m/s) [6], elevated temperatures, and variable stand-off distances from the surface.

3.   Sensitive to critical flaws - including misalignment of fibers and inter-laminar flaws.

4.   Safety, size and weight limitations – to allow ease of implementation and retrofitting to existing AFP technologies.

1.2   Target Defects

The presence of defects, occurring during the manufacturing of parts, can act as initiators for future damage in service. Process parameters of AFP such as the force of consolidation, the speed of layup and the nip-point temperature all influence the occurrence of manufacturing defects such as delaminations, gaps, overlaps, voids and debonding [5]. These defects can be classified into fibre-related (e.g., misalignment of fibers, in-plane waviness, out-of-plane wrinkles, broken fibers), matrix-related (e.g., voids and incomplete matrix cure), interface-related (e.g., fiber/matrix debonding), and delamination type of defects. The out-of-plane wrinkling is considered a defect arising from the manufacturing process which causes a significant degradation to mechanical performance of the composites. The research conducted by Potter et.al. [7] indicates that a clear correlation exists between the strength reduction and the intensity of wrinkling, and can result in a reduction in the strength of up to 50% in compression and up to 70% in tension. Simulated studies show that all plies affected by out-of-plane wrinkling led to a reduction of 72% in stress at initiation of damage [7]. It is common during the formation of multiple plies around a simple radius, for wrinkling to occur since plies cannot slip over one another because of path length differences between the upper and lower side of the ply [8]. The origins of out-of-plane wrinkling can be caused by many other factors and their occurrence is extensively described in [8].

1.3   Advantages of in-line inspection of AFP system

The realisation of in-line monitoring would allow several possible improvements of AFP manufacturing performances, namely:

•   Detect defects at an early stage. It would allow corrections to be made at early stage to reduce wastage of material.

•   Full automation of AFP production and improving manufacturing performance via closed-loop control. The time interval spent between detecting and changing the defected part would be dramatically shortened or ideally automated.

- Build-up of an as-manufactured "digital twin" of parts to help for mechanical modelling predictions. The collected real-world data creates simulations that would inform mechanical models of how they will perform.

1.4   In-line inspection of AFP system

Many authors have approached monitoring and inspection of AFP manufactured plies. There are several initial studies towards in-situ AFP inspection and the main NDE techniques are thermography and profilometry. Some successful implementations of in-line AFP systems were recorded at the early stage by commercial companies such as Flightware [9], Coriolis [10] and Electrimpact [11] for in-line inspection of AFP systems. Juarez et al. [12] recently presented a well-developed thermography inspection technique. Highly sophisticated hardware along with a complex robotic system were exploited to create an advanced inspection system. Recent advances in AFP inspection demonstrated the feasibility of the "*observe-think-react*" approach in [13], showing the potential of the real-time automated fibre placement (RT-AFP) machine in detecting in-plane waviness and preventing it by adjusting the process parameters on-the-go. Various types and sizes of defects should be tested to further develop the proposed RT-AFP machine. A summary of recent advances in in-situ inspection approaches is given in Table 1 .

1.5   The suitable NDE approach for a targeted defect.

One of the more common structural integrity defects in CFRP materials is out-of-plane fibre wrinkles and it is a quite challenging to monitor in real-time. Below a rationale for the interest in investigating ECT over other NDE techniques is summarized.

The most common of these, Ultrasonic testing (UT), can penetrate the bulk of the material, making it suitable to inspect defects such as delamination between the CFRP layers. A challenge in this technique is the need for a coupling medium (often water) or transducer to be in contact with the specimen to transmit ultrasound effectively making traditional UT unsuitable due to pre-requisite 1 (see section 1.1).

A second technique, X-Ray CT, allows the bulk inspection of materials. The limitation of this technique is the size and need for a special environment to contain harmful radiation, making it unsuitable for in-line monitoring from a cost and safety perspective due to pre-requisite 4 (see section 1.1).

4

Electromagnetic Acoustic Transducers (EMATs) generate and detect ultrasound in conducting materials through electromagnetic induction. The technique has good potential for in-situ process monitoring of conductive materials but requires much higher conductivity materials than CFRP to support transmission of ultrasound.

Recent advances in thermographic inspection research presented lock-in thermography (LIT) [14] using miniature infra-red cameras and integrated actuators that offer great potential to employ the proposed LIT on structures for real-time monitoring.

In this study, the targeted defect is out-of-plane wrinkles which is a fibre direction related defect significantly affecting composite material's structural integrity. In practice, the formation of out-of-plane wrinkles may occur during the tow steering process while using AFP at the inside edge of the tow [15]. There is not record of NDE test methods to detect out-of-plane waviness/wrinkles with high signal to noise ratio (SNR) up to date [16]. However, recent research by Mizukami et. al [16] proposed an EC NDE method with improved SNR to the waviness/wrinkle areas by rotating the asymmetric probe angle to be matched with the fibre direction containing waviness.

The eddy current (EC) NDE is based on electromagnetic induction process where the changing magnetic field of the solenoid placed nearby of a conducting material induces the eddy currents (ECs) in an electrical conductor as is shown in Figure 1.a. There are various advantages well-established EC techniques, which are already used for the inspection of fibre-related defects and is one of the most applicable NDE techniques for real-time monitoring of a composite structure [17]–[19]. The first of these is that it is capable of high inspection speeds of composite materials up to 4 m/s [20], [21]. Another advantage is that post-processing of ECT data is not computationally heavy. The third advantage is ECT results are quantitative, making the characterisation of defects related to size, shape, location and depth clearer and traceable. Furthermore, it can operate over a wide frequency range from the kHz up to a 10s of MHz, where the most significant sensitivity to defects within the conductive CFRP is usually expected [22]. A final advantage is that the ECT instrumentation can be made comparatively small in footprint and each device is easily replaceable which means further miniaturization is possible. As a result, ECT was chosen as a suitable NDE technique for in-line inspection. Consequently, the ECT technique is described in the next section for application in AFP monitoring.

Table 1 - Summary of recent advances in AFP inspection

Inspection technique/ NDT Method	Industrial Application	Motivation	Types of defects	Limitations	Advantages	Validation	Proposed in-situ device
Profilometry [9]	100% inspection during continuous production at AFP speed up to 2 m/s	Decreasing the cost of AFP production	Gaps, overlaps, twisted tows and fuzzballs	The location of defects smaller than 0.5 mm	Increase productivity by 20-30% compared to current methods	None.	A line laser and a camera
Thermography [23]	Inspecting areas of insufficient ply adhesion	Limitation of laser profilometry	Laps, gaps, and twists	A lower rate of capture, i.e. low speed of layup	To reduce risk and increase laminate quality during fabrication	None.	An uncooled microbolometer sensor
Thermography [24]	Interruption of AFP due to manual QA (like visual inspection)	Time and cost	Gaps /overlaps, twisted and spliced tows	The computing speed of the developed algorithm limit the real-time capability of the monitoring system.	Online process monitoring system to detect defects for lay-up speeds up to 1 m/sec	None.	IR camera combined with image processing
Thermography [25]	Time-consuming and insufficiency of visual inspection	Time and quality	Tow position, foreign bodies, gaps/overlaps	Cooling tows prior to inspection to create temperature contrast between surface & tows	Localize position of the single lay-up courses in each ply and detect gap width	Comparison between actual and planned positions and estimation of tow and gap widths	A thermal camera
Thermography [26]	Creating more sufficient production environment	Decreasing the cost of inspection	Tow overlap/gap, wrinkling, and peel-up, poor/loss of adhesion between plies and the effects of vacuum debulking	To heat the substrate (base layer) prior to lay up	Capable to detect visually undetectable defects: poor/loss of adhesion between plies, the effects of vacuum debulking	None.	Infrared camera, quartz heating lamp
Thermography [12]	The inspection techniques are ex situ with certain limitations to some type of defects	Detection limitations of certain type of inspection techniques	Gaps, overlapping tows, and Foreign Object Debris	The inspection speed is related to the frame rate of the camera	Enable high-rate AFP manufacturing with minimal interference; novel calibration regime	Comparison with artificial manufacturing induced defects	In Situ Thermal Inspection System
ECT [27]	Automated process monitoring of AFP	Time and cost	Fiber orientations	Penetration depth and resolution.	Applicable on rough surfaces	None.	A differential probe, a half transmission probe (HT) and a high-frequency probe (HF) were tested
The real-time AFP machine (profilometry-based sensors) [28]	Active process control and defect detection during AFP manufacturing	Early defect detection and correction in real-time in AFP manufacturing	In-plane waviness (wrinkle)	The targeted defect size was 3.2 millimetre	The machine can automatically adjust the process parameters to correct the defects	Comparison with a microscopic image	The profilometry-based laser line scanners

1.6 Structure of paper

The objective of this paper is to develop ECT sensors suitable for in-line, real-time quality monitoring and to explore the design parameters of the novel directional ECT probe capable of detecting out-of-plane wrinkles as well as AFP manufacturing flaws for a possibility of in-situ inspection.

The remainder of the paper has the following structure. Section 2 introduces the theory, methods and equipment used, namely: the key EC theory in subsection 2.1 and sensor design in Subsection 2.2. The probe configuration is presented in Subsection 2.3. The significance of probe resonance is evaluated in Subsection 2.4, followed by details of the test samples in Subsection 2.5. The measurement setup and sensor signals are presented in Subsections 2.6 and 2.7, respectively. The modelling approaches is explained in Subsection 2.8. The results & discussion of the simulated and experimental studies are detailed in Section 3. Section 4 concludes with the main findings and future potential of the research.

2 Methods and Equipment

The concept of embedding EC systems into the AFP head is based on the directional probe introduced by Kosukegava et. al [29]. While conventional EC probes are very sensitive to lift-off variation, the hybrid transmit and differential receive (Tx-dRx) nature of the proposed probe enables the sensor to minimize the effect of lift-off due to the movement of the AFP head. Moreover, the unidirectional conductivity of the CFRP layers results in a strong EC densities along the fibre directions of the specimen. Thus, to support the ECs to flow widely and uniformly the uniform driver coil is exploited [29]. The research in the current paper comprises a series of studies to find a suitable configuration from four anisotropic probe designs by testing them on out-of-plane waviness in cured CFRP.

2.1 Eddy current theory

Eddy-Current Testing (ECT) is reliant on Faradays' law of electromagnetic induction where a changing magnetic field will generate eddy currents ECs when incident upon an electrically conductive material. The induced ECs generate their own secondary magnetic field which carries information about the conductivity and magnetic permeability of the test materialand tries to drive its own current in any inductors at the surface. Specific information about the specimen can therefore be revealed by monitoring variations in the electrical properties of the material under the test [30]. The conductivity of carbon fibre allows for the application of ECT techniques for inspecting for CFRP defects [16], [31], [32]. Figure 1 shows one of proposed probe configurations and the expected EC flow based on ECT theory.

Due to the low electrical conductivity of composites, weak detection signal and accuracy is observed in traditional EC inspection. However, by performing high frequency measurements between 100 kHz and 100 MHz, sufficient flow of current is achieved to obtain high-resolution imaging of fibres and other features [33]. In addition, operating probes around electrical resonance enhance the sensitivity of ECT [34].

Directional eddy-current probes with Tx-dRx coils were developed to evaluate the detectability of out-of-plane wrinkling, inspired by directional probes proposed in [29], where the primary magnetic flux is distributed in the area below the probe [35]. Due to the anisotropic nature of the composites, the desired probe configuration is expected to induce ECs to flow along the fibres' orientation, and, by placing differential sensing coils one after another, a strong defect response is possible while minimizing the effects of lift off. The next section provides a detailed explanation of each component of the probe, and the configurations evaluated in the study.

2.2   Directional probe design

A schematic diagram of the proposed probe with its dimensions and relative positions is illustrated in Figure 1. In this study the authors developed and tested the directional EC probe which operated in Tx-dRx modes inspired by Kosukegava et. al [29]. The unidirectional CFRP tape has high conductivity along the fibre direction but low conductivity in the transverse direction, thus, the uniform magnetic field created by the driver coil as is shown in Figure 1 will induce current to flow along with the fibre directions (opposing the direction of coil windings). The rectangular pickup coil is designed with the pickup loop placed orthogonal to the fibre direction such that the defective zone will generate ECs flow in the out-

of-plane direction [36] and the voltage difference between two adjacent pickup coils is then measured as shown in Figure 1. This section provides an explanation of proposed probe design in detail.
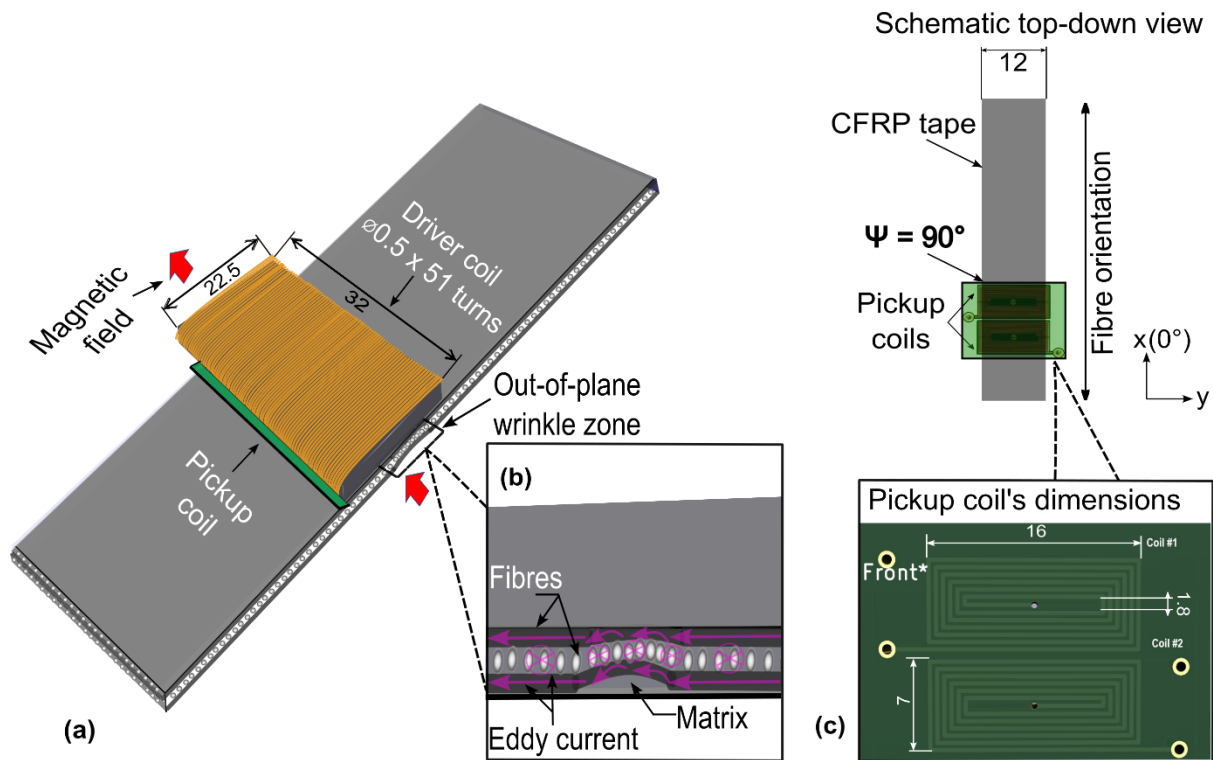

Figure 1. Directional EC probe with asymmetric Tx-dRx coils' dimensions: (a) induction of ECs within a cross-ply CFRP material and dimensions of the directional EC probe design; (b) zoomed in side view of ECs directions; (c) schematic top-down view and rectangular planar pickup coils' dimensions.

2.2.1   Driver coil

The driver coil is hand wound around a rectangular ferrite core (Ferroxcube PLT38/25/3.8-3F4) with 51 turns of 0.5 mm diameter wire as shown in Figure 1. The solid ferrite core increases the primary magnetic flux density around the pickup coils. The dimensions and properties of the driver coil are shown in Table 1. The inductance of both driver and pickup coils were measured using the inductance, capacitance, and impedance meter (PM 6303 RCL, Philips, Netherlands).The targeted inspection width of the AFP based composite is around 12 mm. Thus, it is not necessity for the probe to cover larger areas in this application. The impedance spectra of the coils were obtained by using a Network Analyser (TE3001, Trewmac Systems, Australia).

2.2.2   Pickup coil

The design of the proposed pickup coil consists of two rectangular 12 turns dual layers printed circuit board (PCB) printed coils with 16 x 7 mm dimensions and a distance between the coils of 1 mm. Built on an FR-4 substrate of 1.6 mm height, the traces are 0.3 mm wide with a 0.2 mm pitch, yielding a total of 12 turns on double sides PCB as is shown in Table 2.

Table 2. Material properties and dimensions of the driver and pickup coils.

Driver coil	Parameters and dimensions	Pickup coil	Parameters and dimensions
Number of turns	51	Number of turns	**12**
Wire diameter	0.5 mm	Product Family	2 layer
Dimensions	32.0x22.5x5.5 mm	Copper Weight	35 oz/ft^2
Inductance	102 μH	Thickness	1.6mm
		Material	FR4 (150 deg C) middle Tg
		Circuit Size X	25 mm
		Circuit Size Y	20 mm
		Inductance	1.2 μH
		PCB board dimensions	25x20 mm

2.3 Probe configurations

Due to the unknown relationship between fibre orientation and the electrical properties it is necessary to optimize the relative orientations of driver and pickup coils to increase their sensitivity to perturbations of ECs caused by defects which lead to changes in the secondary magnetic field [28]. Thus, four probe configurations were examined with varying relative orientations of driver to the pickup coils' as is shown in Figure 2. The notation of each probe configuration is based on the following: The fibre direction is classed as 0° and the scanning axis (direction of movement) is always aligned with the fibre direction. Cartesian axes (x, y, z) are defined with x and y in the plane of the composite, and with x aligned to the 0° direction. For all probe configurations considered in this paper, the differential pickup coils are orientated at 90° to the fibre direction i.e. the longer dimension of the coils are perpendicular to the fibres (see Figure 1). The letters "uni" and "non-uni" in the probe naming convention used is denoted by the word "uniform" and "non-uniform", respectively. The first number in the naming convention, either "0" or "90", refers to the primary direction of ECs flow generated by the driver coil, relative to the fibre

direction. Finally, the letter "p" and "o" refers to the parallel and orthogonal orientations of the driver coil B-field relative to the sample, respectively.
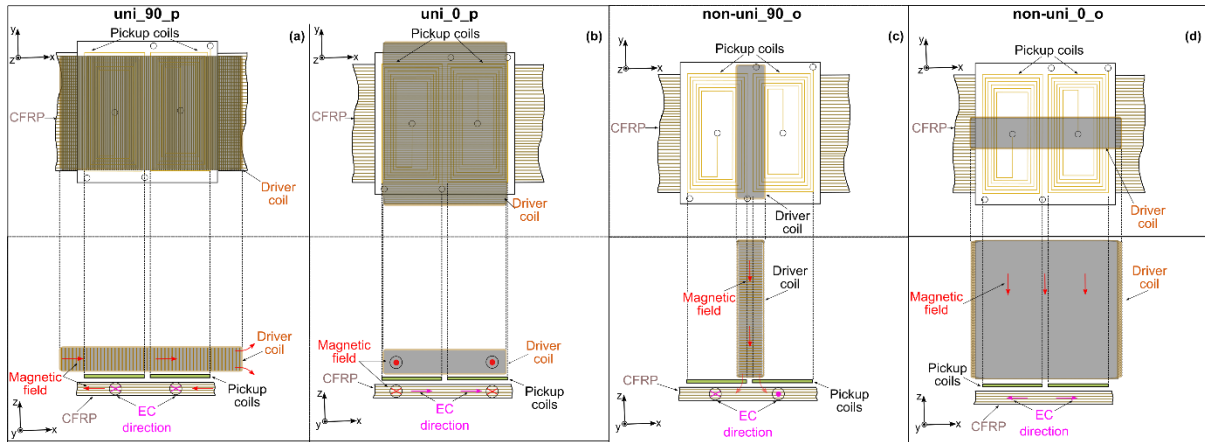

Figure 2. Schematic top and side view of probe configurations (left to right): (a) uni_90_p, (b) uni_0_p, (c) non-uni_90_o and (d) non-uni_0_o probe.

Figure 2 shows cross-ply CFRP specimen with a fiber direction 90° to the scanning axis in the top surface. Probes uni_90_p and uni_0_p generates uniform magnetic fields resulted in uniform ECs induction parallel and orthogonal to the driver coil winding directions as is shown in Figures 2.a and b respectively. In probe uni_90_p (see Figure 2.a) the driver is generating a uniform magnetic field and it is trying to drive currents in a single direction along the fibres resulting in relatively strong current densities generated in the top surface of the sample. The non-uni_90_o probe (see Figure 2.c) is also driving current along the fibres in the top surface but with the driver coil orthogonal to the surface of the sample. Consequently, in this scenario, the ECs flows along the fibres which is expected to generate a much higher EC density. The probes uni_0_p and non-uni_0_o (see Figure 2.b and d respectively) were designed with the driver coil generating ECs across the top surface of the material. So, in the normal position to the surface the excitation coil's non-uniform magnetic field is pointing down and it is driving the current directly beneath the pickup coils.

In the following section these probes will be evaluated on the samples while varying the severity of targeted defect. To begin with Finite Element Modelling (FEM) of the four proposed configurations is

used to virtually test their responses to discontinuities in samples, and the detectability is quantitatively analysed in the following sections.

2.4 Resonance frequencies of probes

The resonance frequencies of both driver coil in air and pickup coils when assembled in the four configurations are shown in Figures 3.a and b, respectively. Based on the findings in [29] optimum sensitivities were observed when the driver and pickup resonant frequencies were comparable. The original resonant frequency of the pickup coils were 13.6 ±0.1 MHz in free space. The resonances of the sensing coils remain consistent due to being PCB manufactured, with only minor difference between peak amplitudes 29±4 Ohms. The driver coil's resonance was equal to 1.59 MHz. Thus, a 10 nF capacitor was used to capacitively load the pickup coils of each probe configuration so that they resonated at 1.5 MHz as is illustrated in Figure 3.b. The calculation for a suggested capacitor value can be found in Appendix A1. Tuning the frequency to below the driver coil's resonance frequencies the system still allowed the measurement of the same structural response from the sample. Based on the findings of [29] this study aims to explore the sensitivity of different anisotropic probe configurations to out-of-plane wrinkling within the range around resonance between 1.4 and 2.3 MHz.
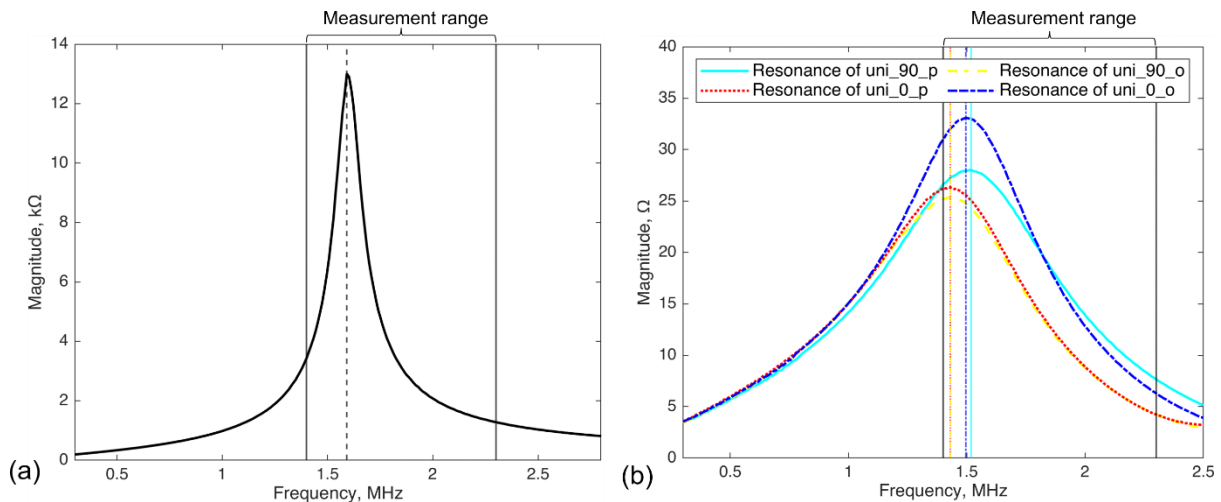

Figure 3. Impedance spectra measurements for: (a) the driver coil in air; (b) pickup coils after 10 nF capacitive loading in the four probe configurations placed on undamaged CFRP.

2.5 Test Samples

A cross-ply CFRP plate of 250 x 25 x 4 mm was fabricated using 32 plies of prepreg (IM7/8552). The layup was $[(90_2/0_2)_4]_s$ and some of the 90-degree plies had strips cut out, and these strips were then stacked between the first two 90 degree plies to create an excess of material over which the 0-degree

plies would then appear wrinkled. The plates were cured in the autoclave using the standard cycle and with the aid of a silicone top plate. For more on the complex laminates seeded with asymmetrical out-of-plane waviness please see the work by Maes et al [37]. In Figure 4.a the G1-3 and G6-G8 specimens are all have wrinkles with increasing amplitude but with asymmetry level around 0.2 mm, however G4-5 and G9 specimens have significant value of wrinkle asymmetry offset. For clarity, in Figure 4.b the G4 sample is measured using the VHX-7000N digital microscope (KEYENCE Ltd., UK) where the offset red vertical line has a maximum amplitude, A, with 0.6 mm offset from the centre line (dashed blue line) of wavelength of the defective zone. The amplitude, or wrinkle height, is shown in Figure 4.c. In addition, aluminum tape was applied to both ends of each sample to act as a datum for the EC scans. The amplitude values of out-of-plane wrinkle along with the skewness for each group (G1-G9) of specimens are given in Table 3.
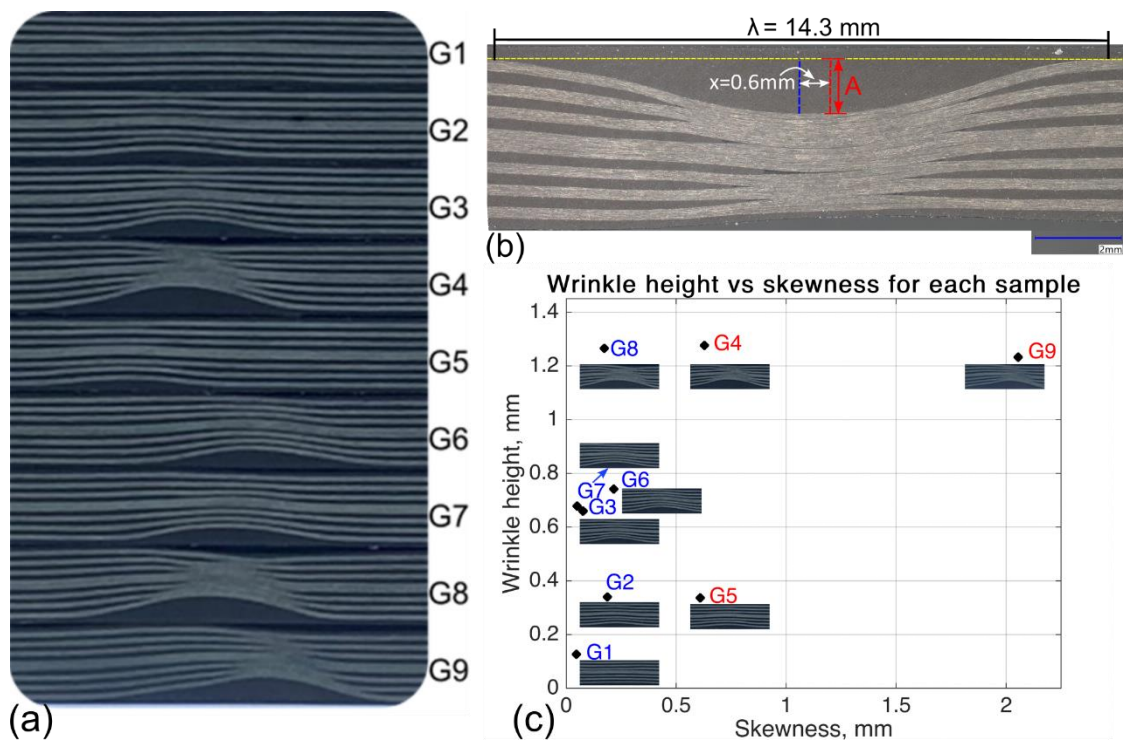

Figure 4. Wrinkle amplitude and skewness for: (a) actual side-view photos of the G1-G9 samples; (b) an example diagram of G7 sample with its wrinkle parameters; (c) plot of each group of specimens in wrinkle amplitude and skewness graph.

Table 3. Micrograph measured values of wrinkle amplitude and skewness for each group of specimens.

Sample	Wavelength [mm]	Height/Amplitude [mm]	Peak offset [mm]
G1	12.44	0.13	0.05
G2	10.19	0.32	0.19

G3	11.39	0.71	0.08
G4	14.36	1.26	0.63
G5	10.31	0.33	0.61
G6	12.17	0.74	0.22
G7	12.35	0.68	0.05
G8	12.85	1.33	0.17
G9	14.85	1.18	2.06

2.6 Measurement Setup

A schematic diagram of the experimental setup is shown in Figure 5.a. A Handyscope HS5 (TiePie Engineering, Netherlands) generates a harmonic sinusoidal excitation signal of frequency f, input to the Howland Current Source (Sonemat Ltd., UK). One output from the current source is connected to the driver coil to provide a consistent current that produces a stable magnetic field at each specific frequency measured. The voltage across the driver coil, V_{mon}, is used as a reference signal for the received pickup signals of the probe. The output coaxial cables from the pickup coils were connected to the inputs of a bespoke differential amplifier (see Figure 6) placed inside the 3D-printed box that houses the entire probe as shown in Figure 5.b. A direct current (DC) power supply 303A (ISO Tech, China) provides a ±5.5 V DC supply for the differential amplifier. A laptop PC and MATLAB script controls and post-processes the measurement in real-time via serial communication with the Handyscope.
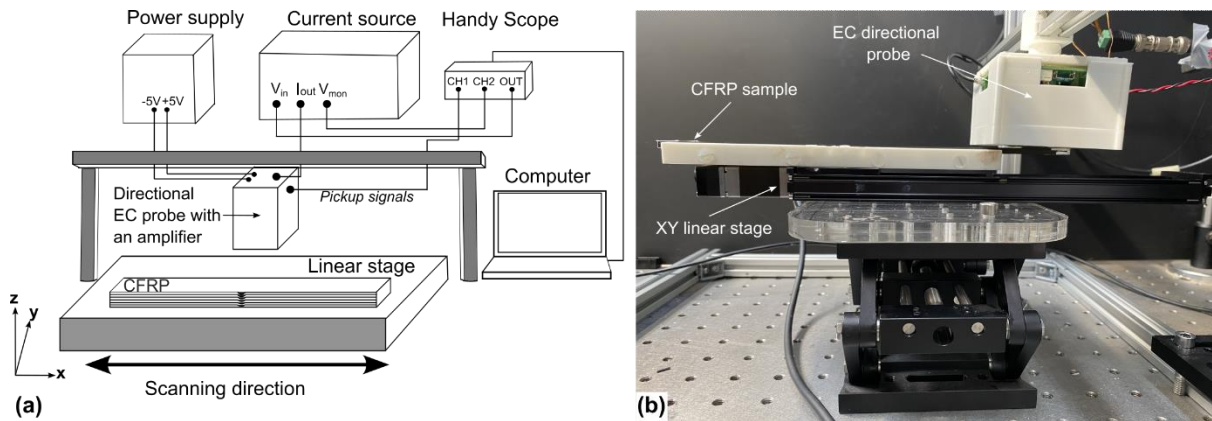

Figure 5. (a) Schematic illustration and (b) actual photo of the probe (side view).

A X-LSM200B-E03 Motorized linear stage (Zaber Technologies, Canada) was used to control the linear movement of the specimen with the probe mounted in a static position. The linear stage was placed on a L490/M Lab Jack (Thorlabs Inc., USA) to control the vertical displacement of the specimen. The lift-off variation was measured using a standard feeler gauge and the level of parallelism of probe and sample were controlled by ruler. The real photo of the probe is illustrated in Figure 5.b. The transformer-coupled differential amplifier developed for this study (see Figure 6) to measure the differential signal

between pickup-coils in the sensors. The reason for the use of an input transformer coupled amplifier, was to allow a differential measurement of the of the two probe coil voltages [i.e. $Vo = Gain\ x\ (V1 - V2)$, where amplifier voltage gain is equal to 10] to be easily and accurately made by simply connecting the two probe coils in series opposition and then connecting them across the non-ground referenced primary of the transformer. This arrangement provides the required balanced loading effect on the two probe coils as is shown in Figure 6.

One of the main challenges in establishing any EC inspection technique set-up is minimizing the noise level. There are many sources of noise which limits the detectability of defects in ECT NDE. As well as random electrical noise, coherent noise is also present from sources that include variations in electromagnetic properties of the sample, temperature changes, probe lift-off and tilt of the sensor. In this study, peak-to-peak signal of the defective region over the root-mean-squared (RMS) value of the coherent background noise is defined as signal-to-noise ratio (SNR) (see Figure 7) and is a suitable metric to quantitatively evaluate probe performance.
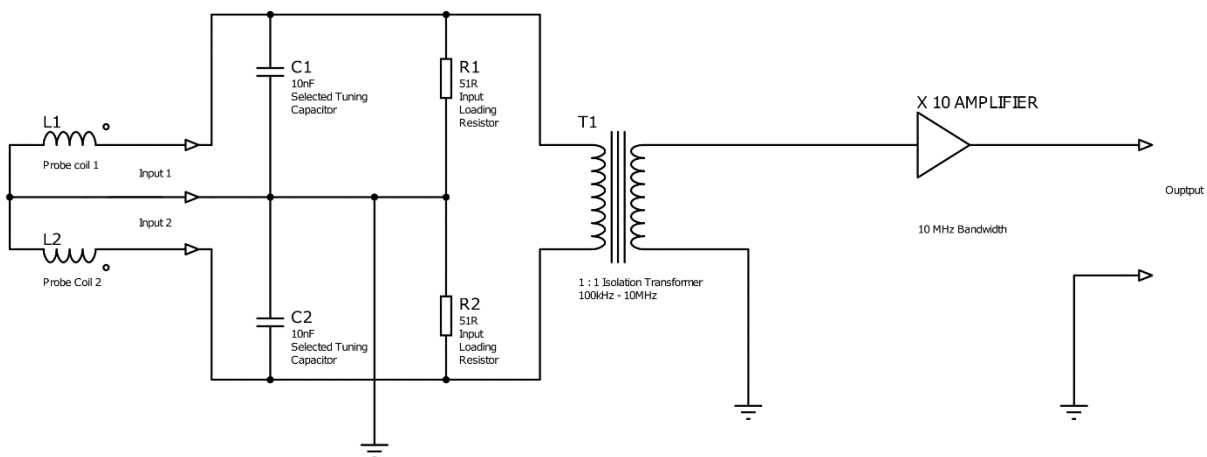

Figure 6. The simplified block diagram of the transformer coupled differential amplifier.

2.7 Sensor signals

Each scan started by moving the stage with a fixed sample on it along the X direction while each probe was recording sensor measurements from the static position. The X-axis linear stage with a fixed sample (see Figure 5.b) is moved by increments of 0.2 mm. Real-time monitoring of the sensor response was performed via MATLAB with a data saving option for further post-processing. The obtained measurement data is used to calculate the SNR by applying detrending to remove unwanted linear measurement trends resulting from minor lift-off variations. An example of a position-based measurement is illustrated in Figure 7. The first 2 mm scan is performed while the sensor was moving

on the sample by increments of 2 μm in the non-defective region and is used to assess the random electrical noise in the measurement. The measurement range between 80-119 mm shows the wrinkle defect signal response (see the vertical blue dashed line in Figure 7.b while the rest of the scan corresponds to the coherent structural information about the sample (referred to as structural noise). The horizontal red dashed lines indicate the 2xRMS noise (see Figure 7.b) of the structural noise. The probe is sensitive to both the structural material background noise and the defective region. Figure 7.c shows example plot of G8 sample's data using four probe configurations.
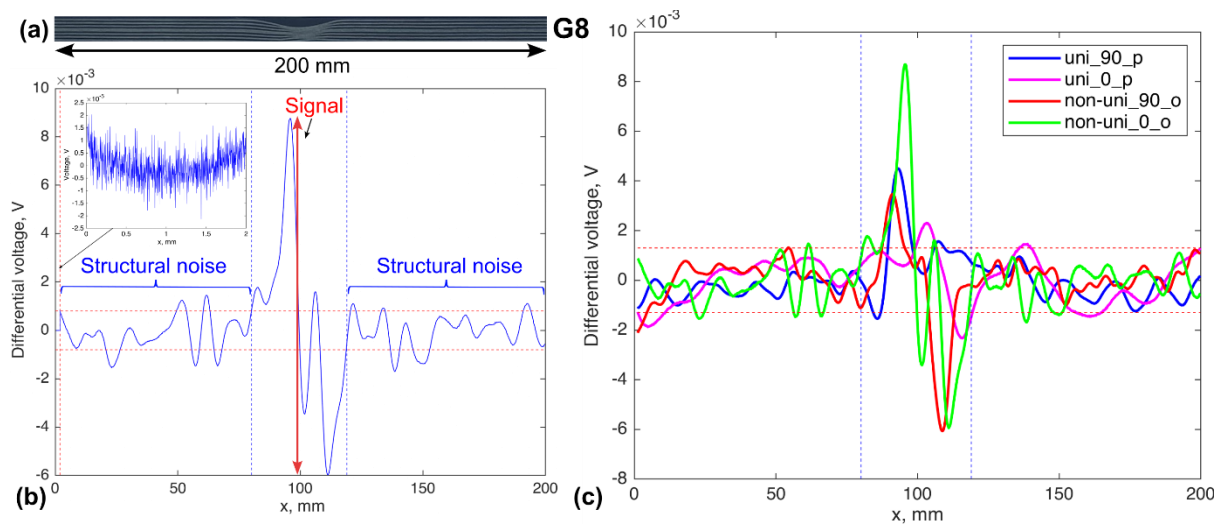

Figure 7 (a). Side view image of CFRP sample, example position-based plot of sample G8 measured at 1.6 MHz using (b) the non-uni_0_o probe showing (in set) sensor and structural noise, and c) four sensor configurations.

2.8 FEM method of low conductivity tensor of CFRP

The CFRP structure is complex, and exhibits electrical anisotropy which can affect the ability of an EC in-line monitoring system to detect defects if not considered. In this section, the modelling approach developed by Yi et.al. [38] is implemented to simulate structural variation in the conductivity tensor representing structural noise. A wrinkle is defined as a region of lower electrical conductivity integrated within the structural model to emulate a realistic coupon sample with a symmetric wrinkle defect. The electromagnetic numerical simulation was developed using COMSOL 5.6 and is shown in Figure 8.a. To investigate the electrical response generated in CFRP, the electrical conductivity tensor must be defined. It should be noted that the σ_L is the conductivity parallel to the fibre direction, σ_T denotes that in the transverse direction and σ_{cp} refers to the cross-ply (through-thickness) conductivity. Therefore,

for unidirectional CFRP, the homogenised conductivity tensor as a function of orientation θ_f (fibre orientation) in a given ply layer can be introduced as follows [39],

$$\sigma = \begin{Bmatrix} \sigma_L\cos^2\theta_f + \sigma_T\sin^2\theta_f & \frac{\sigma_L-\sigma_T}{2}\sin2\theta_f & 0 \\ \frac{\sigma_L-\sigma_T}{2}\sin2\theta_f & \sigma_L\sin^2\theta_f + \sigma_T\cos^2\theta_f & 0 \\ 0 & 0 & \sigma_{cp} \end{Bmatrix}. \tag{1}$$

The tensor modulation method [38] is used to simulate the structural variation of the CFRP laminates. The detailed implementation of the CFRP modelling can be found in [38]. Therefore, by combining the Tx-dRx setup and spatially modulated conductivity tensor the FEM is built. To ensure fast convergence, the coil geometry analysis is first conducted with a relative tolerance of 0.001 and the analysis of the
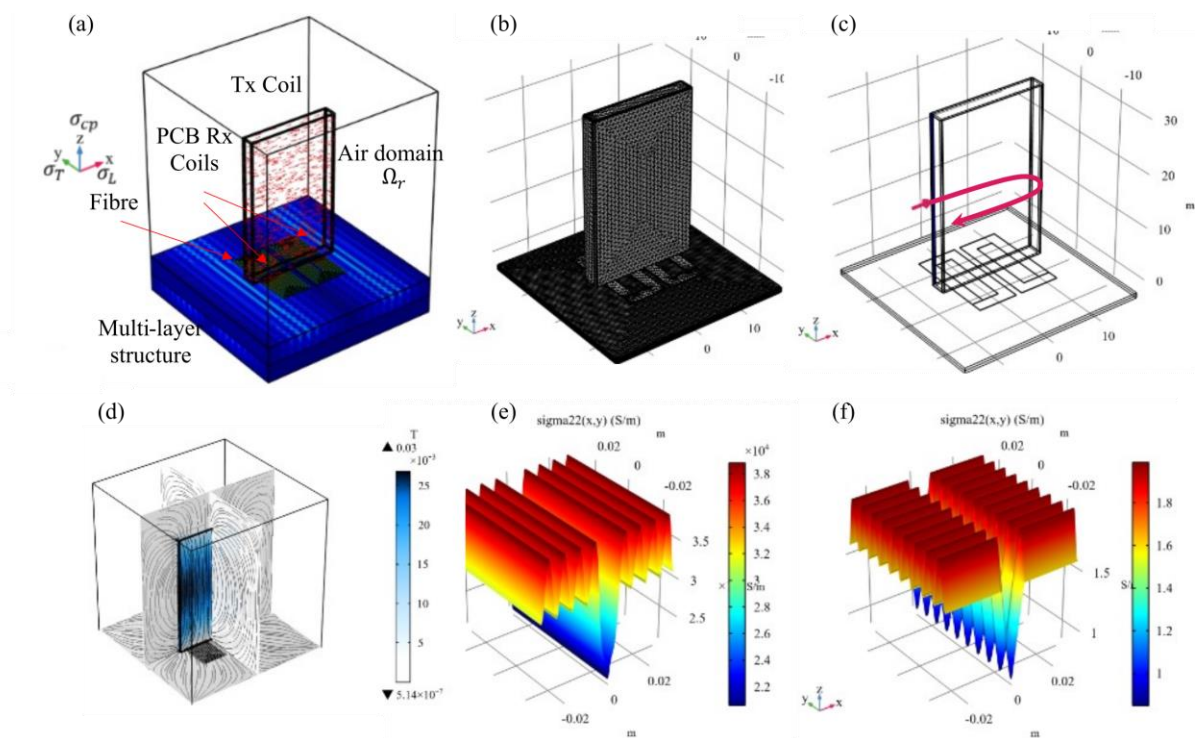

Figure 8. FEM modelling for Tx-dRx ECT system: (a) example solution model, (b) model mesh, (c) numeric analysis of Tx coil gemetory, (d) magnetic flux distribution of Tx coil, (g) σ_{22} of $90°$ layer, (h) σ_{11} of $0°$ layer

frequency domain is conducted in the second stage. Figures 8.b demonstrates the model mesh. The numeric multi-turn homogenized coil model strategy is implemented to simulate the rectangular driving coil, as shown in Figure 8.c, while the arrow denotes the current flow direction.

The whole model has 2,277,196 DOF. The element size was reduced until convergence was achieved. The size of the element ranges from 0.5 mm to 4 mm, depending on position in the model. The whole model is computed on a PC with Ryzen 5900 with 12 cores.

Table 4. Parameters used for FEM modelling.

Parameters	Values
Driving coil	51 turns, 31.75 mm × 20.32 mm × 3.18 mm
Rx coil	12 turns (over two layers), 0.3 mm width and 0.2 mm spacing
Core material	BMHFi-6/23 B
Lift-Off	Rx to sample: 0.1 mm, Tx-Rx: 0.5 mm
σ_L, σ_T	39000 S/m, 7.9 S/m [40], fibre tow wavelength 6.6 mm [38]
Sample thickness	[90/0]₂, each layer is 0.5mm thick.
Wrinkle properties	λ = 10 mm, positioned at each layer. The wrinkle of different severity is simulated as %drop (0% to 75%) of σ at this area
Frequency	1.9 MHz
COMSOL module	AC/DC module
Physics setting in COMSOL	Magnetic fields Electric currents in shells Homogenised multi-turn for coil
FEM study steps	Study1: Coil Geometry analysis Study 2: Frequency Domain study

3 Results & Discussion

A series of studies were conducted to evaluate the sensitivity of Tx-dRx probe configurations and explore the detectability of out-of-plan wrinkling. An example illustration of the simple data processing method used is presented in Appendix B1. The initial study results based on the novel FEM were used to understand how the orientation of the driver coil influences current densities in the top surface and between the layers (at the interface) of the CFRP sample. The first experimental study describes the evaluation of excitation frequency on measurement sensitivity for the 4 probe configurations (see Figure 2), by examining the SNR and measurement uncertainty when measuring wrinkle defect.

3.1 FEM probe configuration analysis

Virtual testing of simulated wrinkles integrated with structural variation of the conductivity tensor [38] is performed. This section quantitatively analyses the performance of each probe configuration using this simulated data.

FEM was used to simulate the four different Tx-dRx configurations (see Figure 9.a-d) above a bi-directional CFRP 2 layer specimen with simulated out-of-plane wrinkling (10 mm wavelength) simulated as material with a reduction in the conductivity of 0% (defect free with modulation) 25%, 50% and 75% compared to unmodulated material with 50% drop of conductivity. The FEM results shown in Figure 9 are the differential voltage between pick-up coil 1 (Rx1) and 2 (Rx2). The previous work mentioned that the effectiveness of the modelling is only validated on the resistive component, therefore simulated data are all real parts of the voltage [38]. The SNR is used to compare the simulated performance of these

configurations based on the peak-to-peak voltage relative to the RMS value of the background structural noise (N_rms), as,

$$SNR = \frac{V_{pp}}{2N_{rms}}, \tag{9}$$

where V_{pp} is the defective voltage (see Figure 7.b. It is noted that all four probe configurations except uni_0_p clearly demonstrate the expected symmetric pattern combined with texture/structure noise and a wrinkle defect response (Figure 9).. It is noted that the simulated fibre tow response (structural noise) is observable in the sound area. Therefore, it is feasible to quantify the SNR using the RMS of the sound area and the wrinkle response from the central conductivity modulated region. The uni_90_p probe appears to exhibit the worst performance for defect detection. Due to the symmetry of the differential pickup coils, the peaks measured by all orientations of the driver coil are symmetric, as shown in Figure 9.a. Parallel configurations induce higher currents on the top surface, while orthogonal probe configurations have higher voltage values on the interface. The voltage values also indicate that a smaller footprint for inducing currents leads to an excellent capability for detecting local wrinkles.

The current densities were analyzed to evaluate the interaction between coils and the sample for the different probe configurations. The current density distribution of the top surface and at the interface (0.25mm depth) were simulated. Firstly, the wrinkle area with lower conductivity is observed at the interface. The highest contrast of current density can be found in the first row of Figure 9.c, where the dominant current axis flows in the direction of fibres and Rx coils are orthogonally aligned. Secondly, exciting samples with the larger area and uniform B-field and the higher current density, as demonstrated in Figure 9.b which has two times large of the current density. Thirdly, when current flows in the $0°$(fibre direction of the second layer), the interface current density is higher than that of the top layer for probes non-uni_0_o and uni_0_p. This effect could be used to excite a stronger electrical response for deep layers in a realistic application.

Each row of Figure 9 shows; i) FEM representation of the four different Tx-dRx probe configurations, ii) the current density magnitude of the top layer $(90°)$, and interface layer $(0°/90°)$ for different probes configurations, and iii) finite element simulation of simulated 1D wrinkle defects scan on [90/0] CFRP structure with varying conductivity drops simulating a wrinkle region. The FEM results show that the uniform magnetic field generates current across the fibers which is not supported in the first layer (see in Figures 9.a-d.ii) resulting in low current densities in the top ply layer for probes uni_0_p and non-uni_0_o. The top surface current densities from FEM may provide information on the suitability of probe

configuration to assess in-plane waviness, whereas the current densities at the interface layers are more desirable to detect out-of-plane wrinkles. Exploring the 4 probe configurations in FEM, allows for the virtual assessment of defect detectability for a given probe configuration. In order to validate the FEM findings, experimental studies were performed on manufactured out-of-plane wrinkles.

3.2 Wrinkle height sensitivity at selected frequencies

Experimental validation was performed to comprehensively evaluate the probe configuration capabilities. Kosukegava et al [29] highlighted the potential for sensitivity improvements in their Tx-dRx probes when operating beyond the resonance of the pickup coil. The experimental study took five repeat scans of sample G9 for each frequency between 1.4 and 2.3 MHz, with increments of 0.1MHz and a 0.2V peak-to-peak excitation voltage. Consequently, the next study shows an evaluation of the detectability of out-of-plane wrinkles for each probe configuration at different frequencies around resonance. The final study shows the relationship between wrinkle height and SNR in the probe configurations.
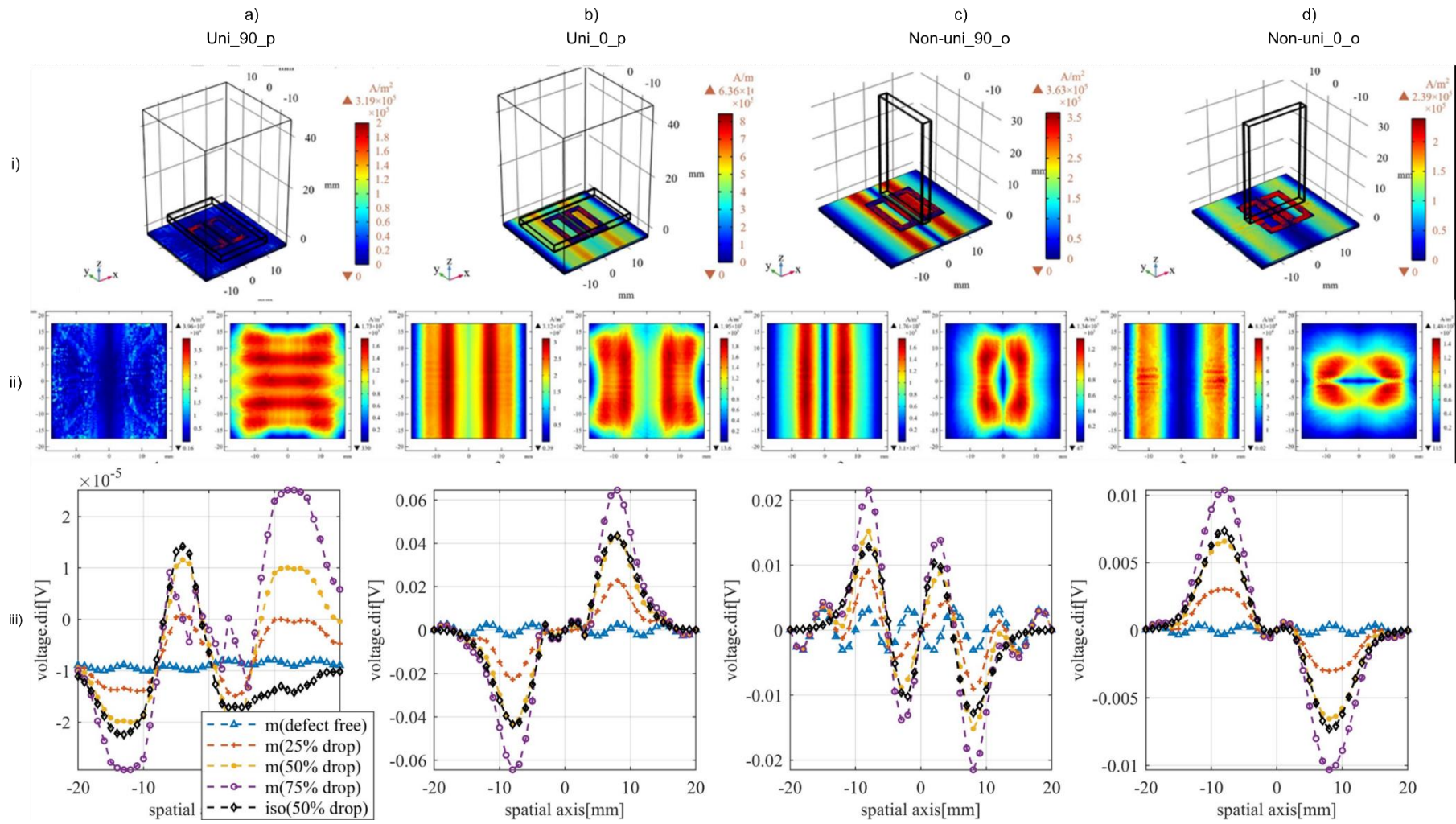
Figure 9. FEM study results for evaluating the best Tx-dRx ECT sensor configuration using: (a) uni_90_p; (b) uni_0_p; (c) non-uni_90_o; (d) non-uni_0_o. i) configuration diagram (FEM), ii) the top surface (left) and interface (right) current densities for each probe, iii) finite element simulation at 1.9 MHz of a simulated 1D wrinkle defect scan on [90/0] CFRP structure for each sensor configuration.
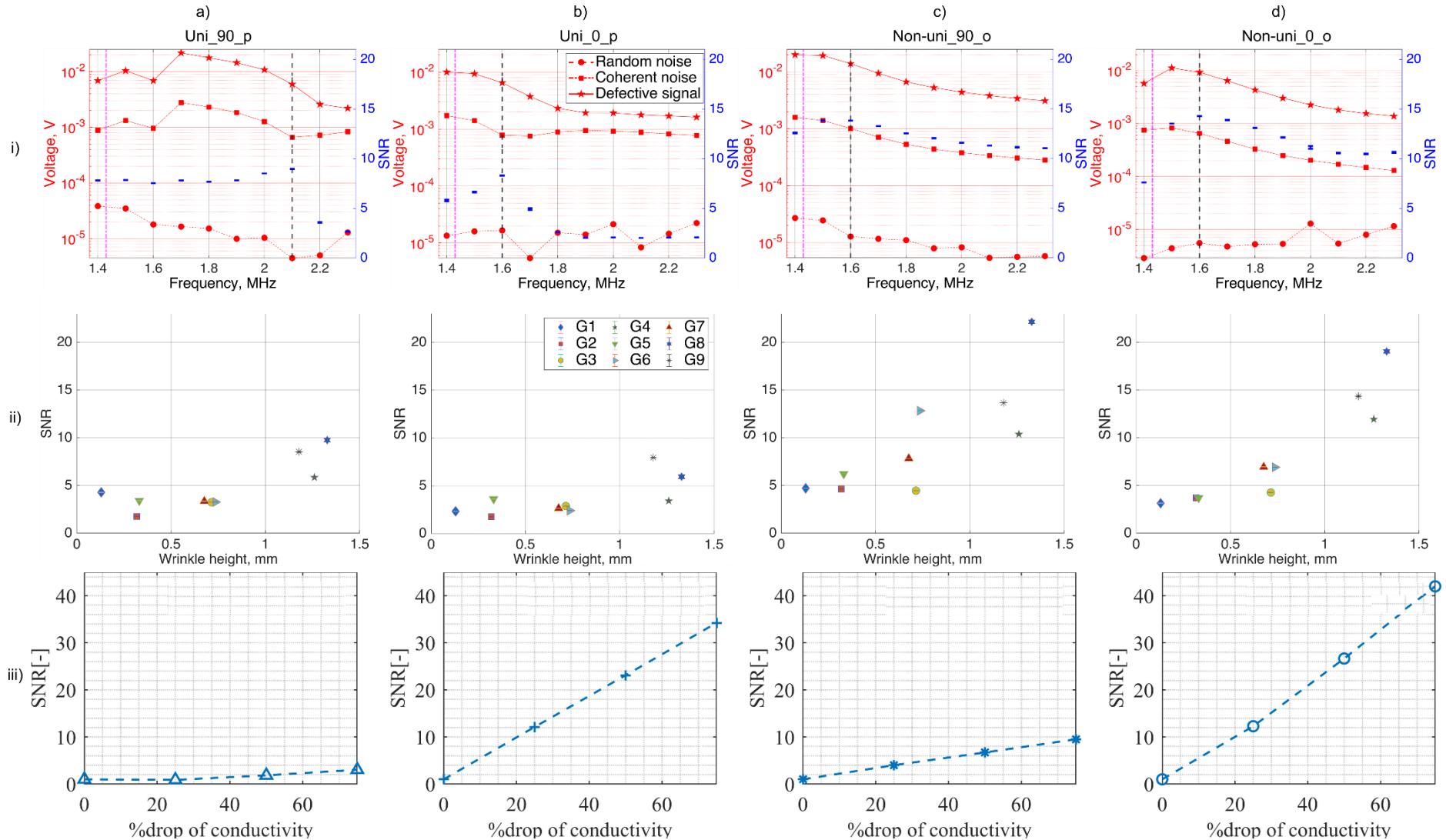
Figure 10. Signal-to-noise results for sensor configurations (a) uni_90_p; (b) uni_0_p; (c) non-uni_90_o; (d) non-uni_0_o. i) Experimental study of response as a function of frequency showing defect signal compared to coherent and measurement (random) noise, and signal-to-noise ratio (blue), ii) signal-to-noise at optimum sensor frequency as a function of wrinkle height, and iii) finite element modelled SNR for changes in conductivity to simulate wrinkles.

The experimental results of the frequency evaluation study are plotted in Figure 10, showing the V_{pp} and N_{RMS} as a function of frequency, along with the random measurement noise contribution. These are compared to the SNR (see equation 9) for a single out-of-plane wrinkle height (sample G9). The highest SNR was found to exist just beyond the resonance of each probe. To evaluate the reason for this peak, the defective signal, probe and coherent noise are shown separately as a function of frequency (the pink vertical line represents resonant frequency of each probe) in Figure 10.i. This demonstrates that for each configuration, the coherent noise and defect signal follow the same trends but a slightly shifted in the frequency domain, such that larger differences in their voltages occur. The coherent background noise was the most significant factor influencing to SNR level at each frequency. The most sensitive probe to coherent noise was found to be uni_90_p, while the most sensitive to defects was non-uni_90_o probe. The diagrams in the second row in Figures 10.ii shows that the probes with the driver coil parallel (p) to the surface of the sample (i.e. generating a uniform magnetic field beneath the pickup coils) achieves lower SNR results than the orthogonal (o) configurations as predicted in the FEM (Figure 10.iii).

The sensitivity to skewness, which has previously been shown by Maes et al [37] to be relevant to the local laminate strength, can be assessed by evaluating wrinkles with comparable height but differing skewness (see Table 4) and by comparing them in terms of their SNR change (see Figure 10.ii). G3/G6 and G2/G5 samples have comparable wrinkle heights but have triple and fivefold increases in terms of skewness value respectively. Non-uni_0_o shows that the SNR for these wrinkles are comparable, while non-uni_90_o probe results show separation in the SNR with increased skewness. However, it is not possible to distinguish between high skewness and low wrinkle height. Based on the experimental results, the most suitable probe for out-of-plane wrinkling detection was the non-uni_0_o, showing a slightly better performance in targeted defect detection in comparison with non-uni_90_o, and insensitivity to skewness. For the simulation study, the best configuration for detecting out-of-plane wrinkles is non-uni_0_o, demonstrating better linearity compared with non-uni_90_o despite the fact that it has a higher SNR value for G9. The uni_0_p and non-uni_90_o probes do not demonstrate the expected performance in the simulated study, which is most likely due to the modelling approach not taking into account the permittivity tensor. Good agreement however, is observed between FEM and experimental study SNR results presented for out-of-plane wrinkles in probes uni_0_p and non-uni_0_o.

As such future work will be able to employ less experimental testing and can implement finite element model optimization of sensor designs.

Conclusion

An eddy-current (EC) directional probe with asymmetric transmit and differential receive (Tx-dRx) coils was designed, constructed and characterized to evaluate the detectability of out-of-plane wrinkling in carbon fibre composite structures. The experimental results were compared to EC Tx-dRx finite element modelling, applying a new spatially-modulated conductivity tensor approach to simulate tow/ply structural noise. The results of the study demonstrate improved signal-to-coherent-noise is achievable through careful selection of the asymmetric driver coil's relative orientation. High-sensitivity to wrinkle-height was achieved when the driver coils primary axis was aligned with the fibre direction, and the driver-coils B-field was orthogonal to the sample surface. In this way, we have demonstrated a potential method for designing real-time ECT monitoring sensors for wrinkle detection in CFRP manufacturing with high SNRs which could have a significant impact on manufacturing rates in smart manufacturing for industry 4.0.

Authorship contributions

Meirbek Mussatayev: Conceptualization, data analysis, methodology and original draft writing - review & editing; Qiuji Yi: Conceptualization, Finite Element Modelling and its draft writing; F, Mark Fitzgerald: amplifier design; Vincent K. Maes: sample preparation; Paul Wilcox: Conceptualization, manuscript

revision, supervision; Robert Hughes: methodology, conceptualization, manuscript revision, supervision.

Declaration of competing interest

The authors declare that they have no known competing financial interests or personal relationships that could have appeared to influence the work reported in this paper.

Data availability

Supporting code and data will be made available at the University of Bristol data repository, data.bris prior to publication.

Acknowledgements

References

[1] P. Alam, D. Mamalis, C. Robert, C. Floreani, and C. M. Ó Brádaigh, "The fatigue of carbon fibre reinforced plastics - A review," *Compos. Part B Eng.*, vol. 166, no. February, pp. 555–579, 2019, doi: 10.1016/j.compositesb.2019.02.016.

[2] C. Yang, Y. Kim, S. Ryu, and G. X. Gu, "Prediction of composite microstructure stress-strain curves using convolutional neural networks," *Mater. Des.*, vol. 189, p. 108509, 2020, doi: 10.1016/j.matdes.2020.108509.

[3] C. T. Chen and G. X. Gu, "Generative Deep Neural Networks for Inverse Materials Design Using Backpropagation and Active Learning," *Adv. Sci.*, vol. 7, no. 5, pp. 1–10, 2020, doi: 10.1002/advs.201902607.

[4] J. Zhang, V. S. Chevali, H. Wang, and C. H. Wang, "Current status of carbon fibre and carbon fibre composites recycling," *Compos. Part B Eng.*, vol. 193, p. 108053, Jul. 2020, doi: 10.1016/j.compositesb.2020.108053.

[5] E. Oromiehie, B. G. Prusty, P. Compston, and G. Rajan, "Automated fibre placement based composite structures: Review on the defects, impacts and inspections techniques," *Compos. Struct.*, vol. 224, p. 110987, Sep. 2019, doi: 10.1016/j.compstruct.2019.110987.

[6] M. Di Francesco, L. Veldenz, G. Dell'Anno, and K. Potter, "Heater power control for multi-material, variable speed Automated Fibre Placement," *Compos. Part A Appl. Sci. Manuf.*, vol. 101, pp. 408–421, 2017, doi: 10.1016/j.compositesa.2017.06.015.

[7] K. Potter, B. Khan, M. Wisnom, T. Bell, and J. Stevens, "Variability, fibre waviness and misalignment in the determination of the properties of composite materials and structures," *Compos. Part A Appl. Sci. Manuf.*, vol. 39, no. 9, pp. 1343–1354, 2008, doi: 10.1016/j.compositesa.2008.04.016.

[8] M. Thor, M. G. R. Sause, and R. M. Hinterhölzl, "Mechanisms of origin and classification of out-of-plane fiber waviness in composite materials — A review," *J. Compos. Sci.*, vol. 4, no. 3, 2020, doi: 10.3390/jcs4030130.

[9] D. Maass, "Progress in automated ply inspection of AFP layups," *Reinf. Plast.*, vol. 59, no. 5, pp. 242–245, Sep. 2015, doi: 10.1016/j.repl.2015.05.002.

[10] G. Gardiner, "Coriolis Composites and Edixia develop inline inspection for AFP," *Composites World*, 2020. https://www.compositesworld.com/articles/coriolis-composites-and-edixia-develop-inline-inspection-for-afp (accessed Jun. 07, 2022).

[11] "Technology - Composites Manufacturing | Electroimpact." https://electroimpact.com/products/composites-manufacturing/technology.aspx (accessed Jun. 07, 2022).

[12] P. D. Juarez and E. D. Gregory, "In Situ Thermal Inspection of Automated Fiber Placement for manufacturing induced defects," *Compos. Part B Eng.*, vol. 220, p. 109002, Sep. 2021, doi: 10.1016/j.compositesb.2021.109002.

[13] D. H. Nguyen, X. Sun, I. Tretiak, M. A. Valverde, and J. Kratz, "Automatic process control of an automated fibre placement machine," *Compos. Part A Appl. Sci. Manuf.*, vol. 168, no. November 2022, p. 107465, 2023, doi: 10.1016/j.compositesa.2023.107465.

[14] G. Ólafsson, R. C. Tighe, S. W. Boyd, and J. M. Dulieu-Barton, "Lock-in thermography using miniature infra-red cameras and integrated actuators for defect identification in composite materials," *Opt. Laser Technol.*, vol. 147, p. 107629, Mar. 2022, doi: 10.1016/j.optlastec.2021.107629.

[15] J. Chen, T. Chen-Keat, M. Hojjati, A. Vallee, M. A. Octeau, and A. Yousefpour, "Impact of layup rate on the quality of fiber steering/cut-restart in automated fiber placement processes," *Sci. Eng. Compos. Mater.*, vol. 22, no. 2, pp. 165–173, 2015, doi: 10.1515/secm-2013-0257.

[16] K. Mizukami, S. Hioki, Y. Takahashi, and K. Ogi, "Experimental and numerical analysis of eddy current sensor signal induced by out-of-plane fiber waviness in carbon fiber composites," *Compos. Part A Appl. Sci. Manuf.*, vol. 163, no. April, p. 107173, 2022, doi: 10.1016/j.compositesa.2022.107173.

[17]   R. R. Hughes, B. W. Drinkwater, and R. A. Smith, "Characterisation of carbon fibre-reinforced polymer composites through radon-transform analysis of complex eddy-current data," *Compos. Part B Eng.*, vol. 148, pp. 252–259, 2018, doi: 10.1016/j.compositesb.2018.05.007.

[18]   D. Wu, F. Cheng, F. Yang, and C. Huang, "Non-destructive testing for carbon-fiber-reinforced plastic (CFRP) using a novel eddy current probe," *Compos. Part B Eng.*, vol. 177, no. September, p. 107460, 2019, doi: 10.1016/j.compositesb.2019.107460.

[19]   P. Zhu, Y. Cheng, P. Banerjee, A. Tamburrino, and Y. Deng, "A novel machine learning model for eddy current testing with uncertainty," *NDT E Int.*, vol. 101, no. October, pp. 104–112, 2019, doi: 10.1016/j.ndteint.2018.09.010.

[20]   M. A. Machado, K. N. Antin, L. S. Rosado, P. Vilaça, and T. G. Santos, "Contactless high-speed eddy current inspection of unidirectional carbon fiber reinforced polymer," *Compos. Part B Eng.*, vol. 168, no. July, pp. 226–235, 2019, doi: 10.1016/j.compositesb.2018.12.021.

[21]   M. A. Machado, K. N. Antin, L. S. Rosado, P. Vilaça, and T. G. Santos, "High-speed inspection of delamination defects in unidirectional CFRP by non-contact eddy current testing," *Compos. Part B Eng.*, vol. 224, no. May, p. 109167, 2021, doi: 10.1016/j.compositesb.2021.109167.

[22]   N. Bowler, "Eddy-Current Nondestructive Evaluation," 2019, doi: 10.1007/978-1-4939-9629-2.

[23]   E. D. Gregory and P. D. Juarez, "In-situ thermography of automated fiber placement parts," *AIP Conf. Proc.*, vol. 1949, no. 1, p. 060005, Apr. 2018, doi: 10.1063/1.5031551.

[24]   B. Denkena, C. Schmidt, K. Völtzer, and T. Hocke, "Thermographic online monitoring system for Automated Fiber Placement processes," *Compos. Part B Eng.*, vol. 97, pp. 239–243, Jul. 2016, doi: 10.1016/j.compositesb.2016.04.076.

[25]   C. Schmidt, B. Denkena, K. Völtzer, and T. Hocke, "Thermal Image-based Monitoring for the Automated Fiber Placement Process," *Procedia CIRP*, vol. 62, pp. 27–32, Jan. 2017, doi: 10.1016/j.procir.2016.06.058.

[26]   P. D. Juarez and E. D. Gregory, "In situ thermal inspection of automated fiber placement manufacturing," *AIP Conf. Proc.*, vol. 2102, no. 1, p. 120005, May 2019, doi: 10.1063/1.5099847.

[27]   C. Schmidt, C. Schultz, P. Weber, and B. Denkena, "Evaluation of eddy current testing for quality assurance and process monitoring of automated fiber placement," *Compos. Part B Eng.*, vol. 56, pp. 109–116, Jan. 2014, doi: 10.1016/j.compositesb.2013.08.061.

[28]   D. H. Nguyen, M. A. Valverde, I. Tretiak, and X. Sun, "In-process detection and automatic response to AFP deposition defects," 2022, no. August.

[29]   H. Kosukegawa, Y. Kiso, M. Hashimoto, T. Uchimoto, and T. Takagi, "Evaluation of detectability of differential type probe using directional eddy current for fibre waviness in CFRP: Advanced Eddy Current Testing for CFRP," *Philos. Trans. R. Soc. A Math. Phys. Eng. Sci.*, vol. 378, no. 2182, Oct. 2020, doi: 10.1098/rsta.2019.0587.

[30]   J. García-Martín, J. Gómez-Gil, and E. Vázquez-Sánchez, "Non-destructive techniques based on eddy current testing," *Sensors*, vol. 11, no. 3, pp. 2525–2565, Mar. 2011, doi: 10.3390/s110302525.

[31]   J. Cheng, J. Qiu, H. Ji, E. Wang, T. Takagi, and T. Uchimoto, "Application of low frequency ECT method in noncontact detection and visualization of CFRP material," *Compos. Part B Eng.*, vol. 110, pp. 141–152, 2017, doi: 10.1016/j.compositesb.2016.11.018.

[32]   K. Mizukami, S. Hioki, K. Moriyama, K. Ogi, W. Miyaji, and K. Kimura, "Eddy-current array-probe technique for imaging near-surface and deep-lying delaminations in multidirectional carbon fiber composites," *Compos. Struct.*, vol. 276, no. June, p. 114537, 2021, doi: 10.1016/j.compstruct.2021.114537.

[33]   S. Hillmann, M. H. Schulze, and H. Heuer, "High-Frequency Eddy Current Techniques," in *Handbook of Advanced Non-Destructive Evaluation*, 2018, pp. 1–28. doi: 10.1007/978-3-319-30050-4_49-1.

[34]   R. Hughes, Y. Fan, and S. Dixon, "Investigating electrical resonance in eddy-current array probes," *AIP Conf. Proc.*, vol. 1706, no. February, 2016, doi: 10.1063/1.4940538.

[35]   H. Kosukegawa, Y. Kiso, J. Horibe, M. Hashimoto, and T. Takagi, "Electromagnetic Nondestructive Inspection of Fiber Misalignment in CFRP with Directional Eddy Current," 2019, Accessed: Jun. 07, 2022. [Online]. Available: http://www.ndt.net/?id=25069

[36]   K. Mizukami, Y. Mizutani, A. Todoroki, and Y. Suzuki, "Detection of in-plane and out-of-plane fiber waviness in unidirectional carbon fiber reinforced composites using eddy current testing," *Compos. Part B Eng.*, vol. 86, pp. 84–94, 2016, doi: 10.1016/j.compositesb.2015.09.041.

[37]   "Maes , V . K ., Elsaied , B . S . F ., Hallett , S . R ., & Kratz , J . (2021). The Effect of Out-of-Plane Waviness Asymmetry on Laminate Strength . In Proceedings of the American Society for Composites — Thirty-Sixth Technical Conference on Composite M," pp. 670–683, 2021.

[38]   Q. Yi, P. Wilcox, and R. Hughes, "Modelling and evaluation of carbon fibre composite structures using high-frequency eddy current imaging," *Compos. Part B Eng.*, vol. 248, no. May 2022, p. 110343, 2023, doi: 10.1016/j.compositesb.2022.110343.

[39]   H. Menana and M. Féliachi, "3-D Eddy current computation in carbon-fiber reinforced composites," *IEEE Trans. Magn.*, vol. 45, no. 3, pp. 1008–1011, 2009, doi: 10.1109/TMAG.2009.2012542.

[40]   G. Wasselynck, D. Trichet, and J. Fouladgar, "Determination of the electrical conductivity tensor of a CFRP composite using a 3-D percolation model," *IEEE Trans. Magn.*, vol. 49, no. 5, pp. 1825–1828, 2013, doi: 10.1109/TMAG.2013.2241039.

Calculation for tuning of the pickup coils

The inductance of each of the pickup coils used in this study is typically around 1.2 μH and they can be tuned to the resonant frequency of the driver coil. To bring the inductance of each coil to electrical resonance at 1.5 MHz (f_0) the following formula should be used to calculate the required capacitance,

$$C = \frac{1}{4\pi^2 f_0^2 L},$$
(A1.1)

where, f_0 is the required resonant frequency in hertz ($1.5 \; MHz$); C is value of the tuning capacitance in Farads; L is the pickup coil's inductance in Henries ($1.2 \; \mu H$).

So, to tune a $1.2 \; \mu H$ inductance pickup coil to $1.5 \; MHz$ operational frequency requires a capacitance $C = 9.38 nF$.

Signal processing of in-line EC data

The simple signal processing of in-line EC data is applied for the given study. The robust method of distinguishing the out-of-plane wrinkle signal from both coherent background noise of the CFRP material and the probe configuration is an important prerequisite to calculate the SNR properly. The data was post-processed to detrend the obtained signal amplitude, the scan positions of the defective signal and coherent background noise zones were identified, and finally the SNR ratio was calculated. The post-processing method can be further justified as a step-by-step algorithm:

- Baseline subtraction
- Detrend
- Peak detection

The experimental EC data has offset from zero. Thus, it was removed by identifying the mean of the experimental data then subtracting the mean value from the experimental. To eliminate any unwanted background trends a low-order polynomial is fitted and subtracted from the signal via polyfit and polyval MATLAB functions respectively. After detrending the signal MATLAB's findpeaks function was applied to find the local peak's width automatically. The peak detection algorithm found the width of peaks that have 3 x RMS whole signal positions. Finally, by multiplying the width of the local maxima of the signal two times the signal positions were defined. The rest of the signal trends were assigned as the structural background noise of the non-defective zone.

The evaluation of sensitivity to the wrinkle area was calculated from the signal to coherent noise. The peak-to-peak value of the signal positions divided by the 2 x RMS value of the coherent noise structural noise .

Figure 7.c shows the example plot results of G8 sample using signal processing of in-line EC data. The signal starts and ends indexes (see the vertical blue dot lines in Figure 7.c) were identified by finding the cross section between the mean RMS values of coherent structural noise and the width of the local peak. The maximum and minimum noise threshold were defined by two time multiplication of the mean of RMS noise value at each frequency for selected sample (see parallel blue dote lines in Figure 7.c).